Chemical Science

Accepted Manuscript

Chemical Science

rsc.li/chemical-science

Volume 9
Number 1
7 January 2018
Pages 1-268

ISSN 2041-6539

EDGE ARTICLE
Xinjing Tang et al.
Caged circular siRNAs for photomodulation of gene
expression in cells and mice

ROYAL SOCIETY
OF CHEMISTRY

rsc.li/chemical-science

ARTICLE

Rational phosphating layer design in biomass-derived hard carbons toward fast charging capability of sodium ion battery anodes

Haihan Zhang, [a] Zhenxin Huang, [a] Siyuan Lin, [a] Jiawu Cui, [a] Qianyu Zhang,*[c] Xiansheng Luo, [d] Rui Wang, [d] Chaofeng Zhang,*[d] Chengyong Shu [a] and Wei Tang *[ab]

Continuous side reactions between the biomass-derived hard carbon surface and the electrolyte affect its cycling stability and fast-charging performance. Therefore, constructing a stable solid electrolyte interface (SEI) while facilitating easier desolvation of sodium ions in the electrolyte is key to achieving stable fast charging. Theoretical calculations confirm that Na_3P can induce the formation of a Na^+ solvation structure with low solvent coordination, thus achieving a lower desolvation energy barrier and faster Na^+ diffusion capability through the SEI. We used bamboo powder, partially de-lignified, as a precursor for hard carbon. After sublimating red phosphorus in a sealed tube and cooling deposition, a phosphide layer was constructed on the hard carbon surface. During charge-discharge cycling, a SEI enriched with Na_3P components was formed on the surface. The final full cell assembled with HC-3wt% P matched with the cathode exhibited excellent rate performance, with a reversible discharge capacity of 78 mAh g^{-1} at 10 C, significantly outperforming the performance of recently reported bamboo powder-based hard carbon. The assembled pouch cell maintained stable cycling for 1000 cycles at 0.5 C. This work provides guidance from the perspective of SEI regulation and design for enhancing the fast-charging performance of biomass-derived hard carbon anodes in sodium-ion batteries.

Introduction

Under the global transition of the energy structure, the renewable energy generation and electric vehicle industries are experiencing rapid growth, leading to an increasing demand for large-scale energy storage technologies.[1, 2] Sodium-ion batteries, due to their abundant resources, low cost, and environmental friendliness, have emerged as one of the strongest candidates for the next generation energy storage systems.[3, 4] Nevertheless, the commercialization of sodium-ion batteries is still fraught with numerous challenges, among which the performance limitations of the anode materials are particularly prominent. Hard carbon materials, owing to their advantages of low cost, high sodium storage capacity, and good cycling stability, have garnered significant attention for anode materials in sodium-ion batteries.[5, 6]

In recent years, biomass-derived hard carbon materials showcased immense potential in the realm of anode materials for sodium-ion batteries, primarily owing to their abundant availability, renewability, and tunable structure.[7, 8] Biomass precursors, such as lignin, cellulose, and the like, possess rich natural porous structures and heteroatoms (e.g., oxygen, nitrogen), which, after carbonization,

can form hard carbon materials with distinctive microstructures and surface chemical properties.[9, 10] However, when it comes to fast-charging applications, biomass-derived hard carbon materials still encounter a myriad of challenges. For instance, the diversity of biomass precursors leads to significant structural variations in the carbonized products, making it difficult to precisely control performance.[11, 12] Additionally, the intrinsic conductivity of hard carbon materials is low, limiting their electrochemical performance at high rates.[13, 14] Furthermore, side reactions between the hard carbon surface and the electrolyte can also compromise their cycling stability and fast-charging capabilities.[15, 16] Therefore, how to enhance the fast-charging performance of biomass-derived hard carbon anodes through rational structural design and surface modification strategies has become a critical issue that needs to be addressed in current research.

Recent studies on biomass-derived hard carbon and fast charging of graphite anodes have provided valuable insights that can be leveraged to enhance the fast- charging performance of biomass-derived hard carbon anodes. Chen et al[17] exposed the free radicals in natural bamboo by appropriate lignin removal, and the abundant free radicals facilitated the utilization of precursor fragments during the carbonization process, leading to the formation of a developed carbon layer with substantial closed pores. This structural characteristic enabled the hard carbon to achieve an optimal reversible capacity of 350 mAh g^{-1} under a current density of 20 mA g^{-1}. However, its reversible capacity significantly decays to only 60 mAh g^{-1} when subjected to a high current density of 1000 mA g^{-1}. Although the removal of lignin alone proved beneficial for the initial reversible capacity of bamboo-based hard carbon, the rate capability of this material still fell short of the requirements for fast - charging

a. School of Chemical Engineering and Technology, Xi'an Jiaotong University, Xi'an, 710049, China. Email: tangw2018@xjtu.edu.cn
b. National Innovation Platform (Center) for Industry-Education Integration of Energy Storage Technology, Xi'an Jiaotong University, Xi'an, 710049, China.
c. College of Materials Science and Engineering, Sichuan University, Chengdu, 610064, China. Email: zhangqianyu@scu.edu.cn
d. School of Materials Science and Engineering, Anhui University, Hefei, 230601, China. Email: cfz@ahu.edu.cn
Supplementary Information available: [details of any supplementary information available should be included here]. See DOI: 10.1039/x0xx00000x

anodes. Notably, Sun et al [18] proposed that the SEI components play an important role in the desolvation of alkali metal ions during fast charging. Their findings revealed that SEI materials with higher Li^+ adsorption energy were capable of achieving faster desolvation processes. By constructing an ultrathin phosphorous layer on the graphite surface, they orchestrated an in-situ transformation to a crystalline Li_3P-based SEI with high ionic conductivity.

Drawing inspiration from research on interfacial construction for fast-charging anodes, the ideal SEI for fast-charging anodes is designed to be thin and have high Na^+ conductivity, which supports the rapid transport of Na^+ at the electrode surface. Herein, Following the sublimation of red phosphorus and subsequent cooling deposition, a phosphide layer was constructed on the surface of the hard carbon derived from de-lignified bamboo powder as a precursor. During charge-discharge cycling, an SEI rich in Na_3P

components was formed on the surface, while a solvation sheath with a low solvent coordination number could form near the inner Helmholtz plane (IHP) at the Na_3P interface, thereby supporting rapid Na^+ desolvation. Moreover, by inhibiting the continuous reduction of the electrolyte at the anode surface, a thinner and more homogeneous SEI layer is generated, resulting in a full cell composed of an $O3$-$NaNi_{1/3}Fe_{1/3}Mn_{1/3}O_2$ cathode. Consequently, this $O3$-$NaNi_{1/3}Fe_{1/3}Mn_{1/3}O_2$//3wt%P HC full cell exhibits excellent rate performance, with a reversible discharge capacity of 78 mAh g^{-1} at 10C, significantly outperforming recently reported bamboo powder-based hard carbon. Moreover, the assembled pouch cell can maintain stable cycling for 1000 cycles at 0.5 C, demonstrating the feasibility of this method for the commercial application of hard carbon anodes.
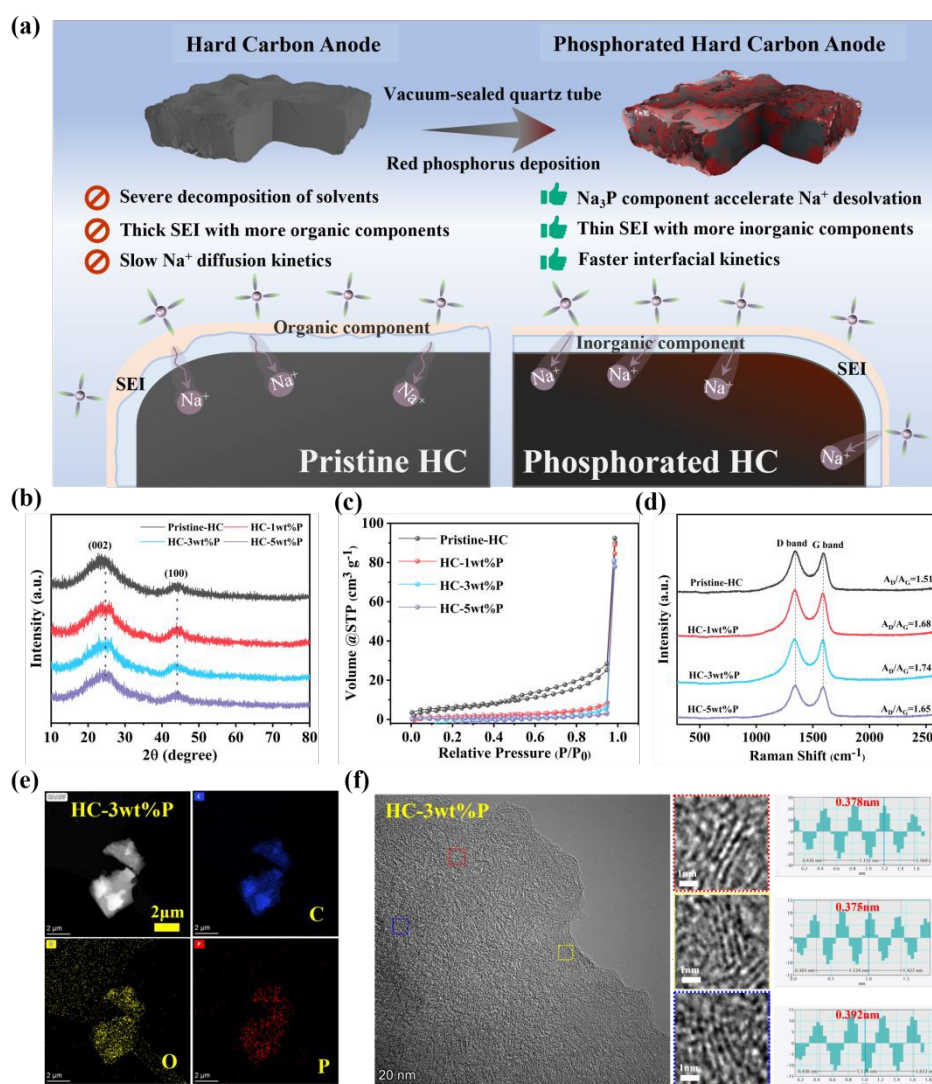

Fig. 1 Synthesis and structural features. (a) Schematic diagram of preparing phosphorated hard carbon anode and working mechanism of phosphating layer design. (b) XRD patterns of all as-prepared samples. (c) N_2 adsorption–desorption isotherms. (d) Raman spectra. (e) HAADF-TEM images and element mapping of C, O, P of HC-3wt%P. (f) HRTEM images of HC-3wt%P.

Journal Name

ARTICLE

Results and discussion

The phosphide layer of bamboo powder-based hard carbon is formed through the sublimation deposition of red phosphorus as illustrated in Figure 1a. During the charge-discharge process, a solid electrolyte interphase (SEI) enriched with Na_3P components is generated, which contributes to the hard carbon anode's superior electrochemical performance.[19] Figure 1b compares the X-ray diffraction (XRD) results of the original bamboo powder-based hard carbon and the hard carbon composites with varying mass percentages of red phosphorus (Figure 1b), all samples exhibit two broad peaks around 23° and 44°, corresponding to the 002 and 100 crystal planes of graphite, indicating that the samples retain the typical amorphous structure of hard carbon.[20] Moreover, the (002) peak shifts to a lower angle with increasing red phosphorus content, indicating that phosphidation enlarges the interlayer spacing of the graphite domains within the hard carbon. Furthermore, the N_2 adsorption-desorption isotherms (Figure 1c and Figure S1, Supporting Information) show that the specific surface area of the red P/hard carbon composites is significantly smaller than that of the original hard carbon (original hard carbon: 23.2 m^2 g^{-1}; 1wt%P, 3wt%P, and 5wt%P phosphated hard carbon: 6.73, 4.46 and 2.53 m^2 g^{-1}, respectively). Pore size analysis of the samples, conducted using the Barrett-Joyner-Halenda (BJH) method as shown in Table S1, indicates that the average pore size of the phosphated hard carbon is approximately 1.5 nm, smaller than that of the original hard carbon (3.7 nm).[21, 22] The reduction in specific surface area and average pore size indicates that red phosphorus successfully deposited on the

surface of hard carbon, partially occluding its pores. According to the X-ray photoelectron spectroscopy (XPS) shown in Figure S4 (Supporting Information), the phosphated hard carbon exhibits a characteristic peak of P around 130 eV compared to the original hard carbon. A detailed analysis of the high-resolution P 2p spectrum reveals peaks centered at 130 and 130.7 eV, corresponding to P $2_{P3/2}$ and P $2_{P1/2}$, respectively. Additionally, peaks at 131.6 and 134.3 eV are attributed to P-C and P-O-C bonds, respectively. These findings suggest that red phosphorus successfully forms a composite with hard carbon through robust chemical interactions.[23]

Small-angle X-ray scattering (SAXS) has been further employed to analyze the closed pore characteristics that are not detectable by N_2 adsorption as shown in Figure S2 (Supporting Information). A plateau in the intensity variation is observed at 0.1 Å^{-1}, which can be attributed to the presence of closed pores within the carbon structure.[24, 25] In this region, the scattering intensity of the original hard carbon is notably higher than that of the 3wt%P-HC, indicating that the original hard carbon contains more closed pores. These closed pores facilitate the intercalation and insertion of sodium ions, contributing to sodium storage within the plateau region of the electrochemical profile. However, this structural feature is disadvantageous for rapid sodium storage kinetics,[26] while partial embedding of phosphorus into the carbon framework enlarges the interlayer spacing and diminishes the number of stacked closed pores, thereby improving rapid sodium storage.[27]
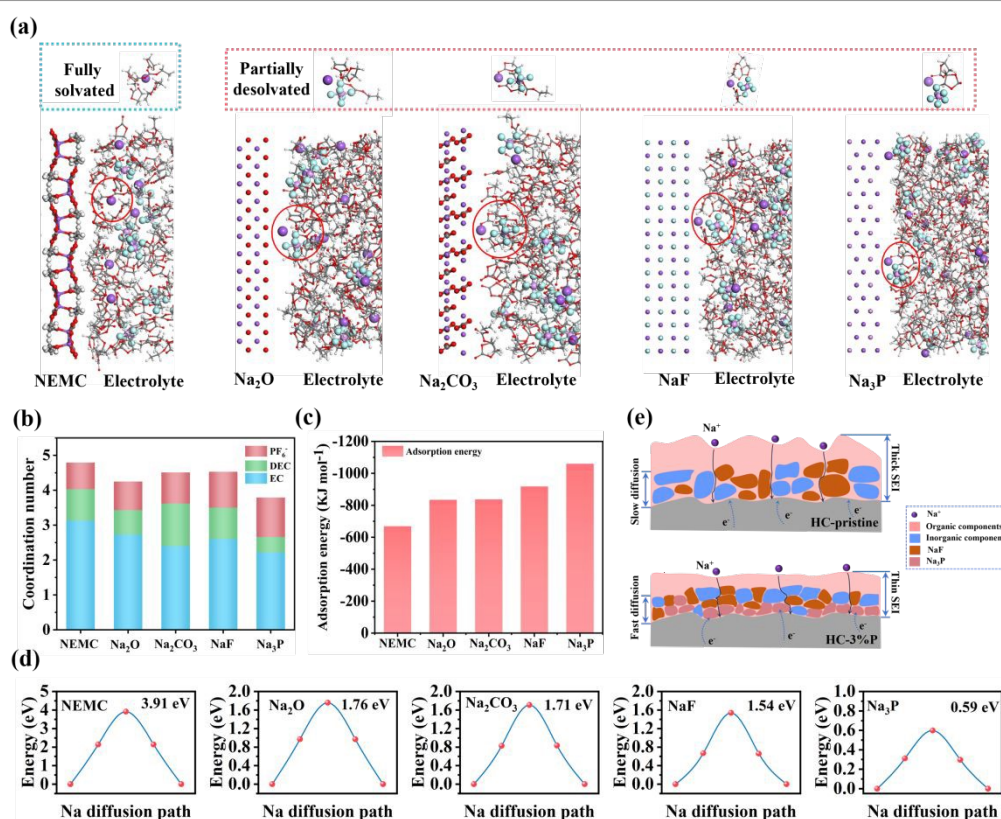
Fig. 2 The theoretical investigation on the desolvation process of Na^+ within (a) NEMC, Na_2O, Na_2CO_3, NaF and Na_3P based SEI. (b) Coordination number of the solvation structure near the IHP on various SEI species based on the MD simulation results. (c) The adsorption energy of various SEI components for Na^+. (d) The Na^+ transfer energy barrier on NEMC (100), Na_2O (111), Na_2CO_3 (101), NaF (111) and Na_3P (101) surface. (e) Schematic diagram of Na^+ across through different anodes SEI.

ARTICLE

Compared to the original hard carbon (Figure S5a, Supporting Information), the transmission electron microscopy (TEM) images and corresponding elemental mapping (Figure 1e) of the 3wt%P-HC further corroborate the uniform distribution of phosphorus on the surface of the hard carbon. Scanning electron microscopy (SEM) images (Figure S6, Supporting Information) reveal that all the hard carbon morphologies are irregular block-like shapes, with the distribution of red phosphorus in the 5wt%P-HC showing some degree of aggregation and unevenness. Further analysis of the graphite crystallite structure before and after phosphidation using high-resolution transmission electron microscopy (HRTEM) illustrates that the interlayer spacing of graphite crystallites in 3wt%P-HC (0.375-0.392 nm) is larger than that of the original hard carbon (0.356-0.378 nm) (Figure 1f and S5b, Supporting Information). This indicates that the bonding of red phosphorus with hard carbon has expanded the interlayer spacing of graphite crystallites, which is beneficial for the rapid insertion and extraction of Na^+ in phosphated hard carbon.[28, 29] Figure 1d depicts the Raman spectra of several hard carbon samples, and Figure S3 (Supporting Information) illustrates the peak fitting results. By calculating the peak area ratio of the D band at 1350 cm^{-1} and the G band at 1570 cm^{-1} in the Raman spectra of the HC samples (Figure 1d and Figure S3, Supporting Information), it is evident that the AD/AG ratio increases in the phosphated anodes compared to the original hard carbon. This observation indicates that red phosphorus penetrates the carbon framework, thereby enhancing the degree of amorphization and introducing point defects within the structure.[30]

By integrating molecular dynamics (MD) simulations with density functional theory (DFT), this study investigates the effects of conventional solid electrolyte interphase (SEI) components (including organic constituents, Na_2O, Na_2CO_3, and NaF) as well as Na_3P on the Na^+ solvation structure at the electrode-electrolyte interface. The findings further unveil the primary reasons for the enhanced Na^+ transport kinetics observed in biomass-derived hard carbon featuring a phosphated layer. Figures 2a and S8 depict the utilization of molecular dynamics (MD) simulations to compare Na_3P with conventional SEI components, including organic components (sodium ethylene monocarbonate, NEMC) and inorganic components (Na_2O, Na_2CO_3, and NaF), in terms of their influence on the Na^+ solvation structure at the anode interface.[31-33] Based on the computed radial distribution function, the Na^+ solvation structures near the inner Helmholtz plane (IHP) were analyzed (as shown in Figure 2b and Figure S9, Supporting Information).[34, 35] For the Na^+-O (ethylene carbonate (EC)/diethyl carbonate (DEC)) and Na^+-P (PF_6^-) pairs, the primary peaks of g(r) appear at 2.4 Å and 3.2 Å, respectively. Among all SEI components, EC exhibits a significantly higher coordination number than DEC and PF_6^-. Among all these solvated interfacial systems, Na^+ undergoes partial desolvation on the Na_3P surface, exhibiting the lowest coordination number of 3.79. Na^+ with lower solvent coordination is more prone to desolvation before diffusing through the SEI.[36, 37] On the interface of organic component NEMC, Na^+ is almost entirely solvated by approximately 3.13 EC molecules and 0.9 DEC molecules, with the lowest number of PF_6^- ions (0.76) in the solvation shell. Furthermore, compared to

NEMC, Na^+ exhibits an even lower coordination number on the surfaces of Na_2O, Na_2CO_3, and NaF.

Figure 2c presents the density functional theory (DFT) calculations of Na^+ adsorption behavior on different SEI components (Figure S7, Supporting Information). Na_3P exhibits the strongest adsorption energy for Na^+ resulting in distinct Na^+ solvation structures near the IHP at the anode interface. The calculations reveal that Na^+ could easily undergo desolvation on the Na_3P surface.[38, 39] Furthermore, as shown in Figures 2d and S10 (Supporting Information), the diffusion energy barriers of Na^+ on different SEI component crystal facets were computed and analyzed. An exceptionally low Na^+ diffusion energy barrier of only 0.59 eV is observed on the Na_3P (101) surface. In contrast, Na^+ diffusion on the NEMC (100) surface requires a significantly higher energy barrier of 3.91 eV (Figure 3d). In order to more clearly understand the effects of different SEI components on the solvation structure and sodium ion transport kinetics, the summary data is shown in Table S2. Combining the above MD and DFT calculation results, the construction of a phosphide layer, as illustrated in Figure 2e, facilitates Na^+ desolvation, reduces continuous electrolyte consumption, and leads to the formation of a thinner SEI enriched with inorganic components.[40-42]

To elucidate the practical role of phosphorization treatment in enhancing the electrochemical performance of bamboo powder-derived hard carbon anodes, half-cells using different hard carbon materials as working electrode and sodium metal as counter and reference electrodes are used for electrochemical characterizations. Firstly, the HC-3wt%P anode exhibited a contact angle of 11.3° with the electrolyte (commercial 1 M $NaPF_6$ in EC/DEC (v/v = 1:1)) (Figure 3a), significantly lower than that of pristine-HC (26.6°), suggesting enhanced wettability. Which expanding the electrode/electrolyte contact area and reducing the interfacial charge transfer impedance. In addition, more uniform electrolyte infiltration promotes the growth of dense SEI in the first cycle, effectively inhibiting side reactions and interface instability. Moreover, the initial charge-discharge curves at 0.1 C (Figure S11, Supporting Information) indicate that with increasing phosphorization content, the initial discharge capacity increases, which should be attributed to the reaction between sodium metal and the phosphide layer, forming Na_3P components in the SEI. Despite a marginal reduction in the initial Coulombic efficiency (ICE), the HC-3wt%P anode (ICE = 82%, 293 mAh g^{-1}) retains a reversible capacity nearly comparable to that of the pristine-HC anode (ICE = 88%, 291 mAh g^{-1}).

Further analysis of the second-cycle charging process (Figure 3b) reveals that with an escalating phosphorization content, the contribution of reversible capacity in the high-voltage sloping region (relative to Na^+/Na > 0.1 V) increases.[43, 44] The HC-3wt%P anode exhibits the highest sloping-region capacity contribution at 52.2%, compared to 48.5% for the pristine-HC anode. Since the enhancement of capacity in the sloping region facilitates rapid sodium storage, the phosphorized hard carbon exhibits superior rate performance (Figure 3c, 3d) in comparison to pristine-HC. At current densities of 30, 60, 150, 300, 600, and 1200 mA g^{-1}, the HC-3wt%P anode maintains relatively high capacities of 286, 270, 256, 242, 228, and 206 mAh g^{-1}, respectively, with the capacity retention from 0.1 C to 4 C rate testing also improves from 54.9% for pristine HC to 72.7% (Figure S12a, Supporting Information). The poor reversibility of
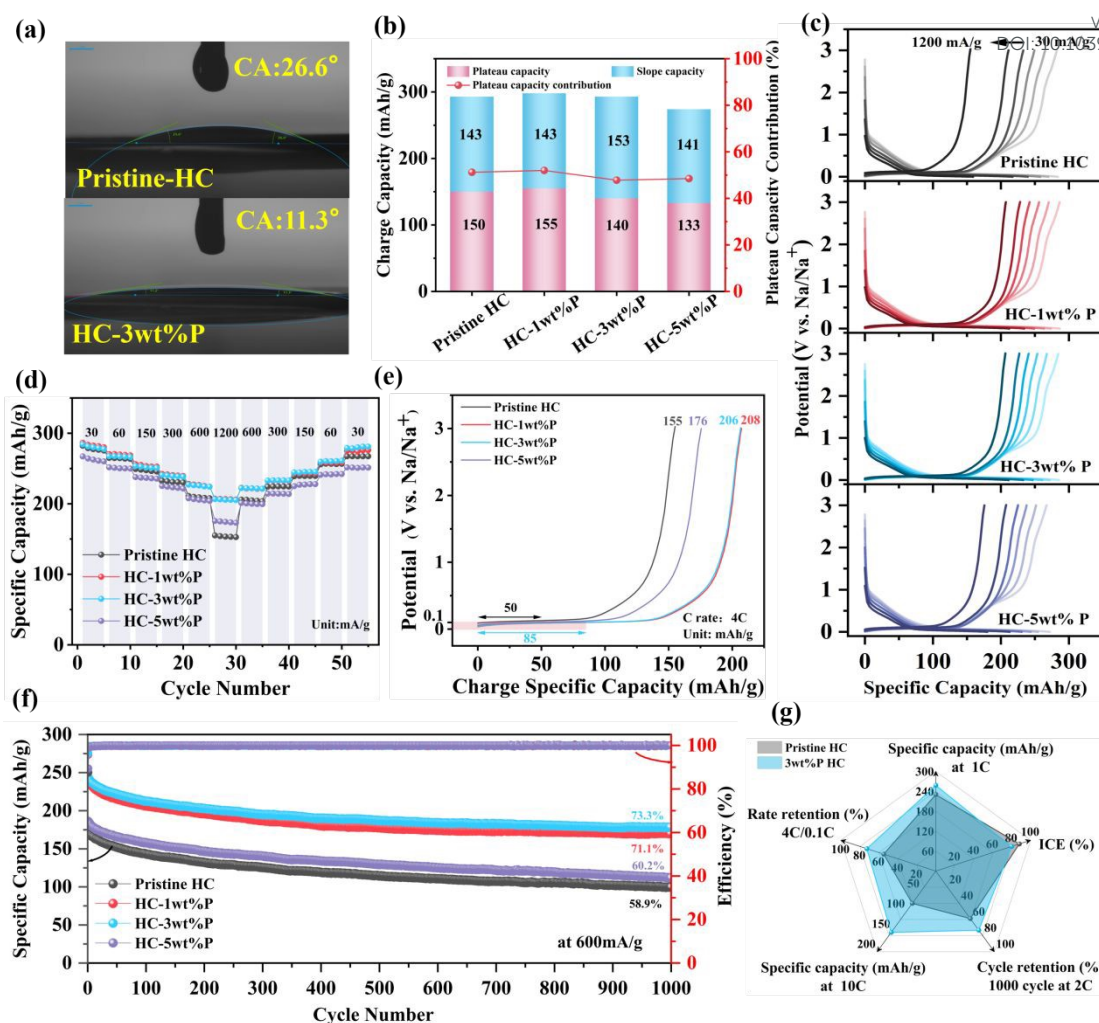
ARTICLE

Fig. 3 Electrochemical performance of the phosphatized HC anodes. (a) Apparent contact angle between electrode material and electrolyte. (b) Comparison between sloping capacity and plateau capacity of samples based on the second charge curves at 30 mA g⁻¹. (c) The GCD curves of samples at current densities of 30-1200 mA g⁻¹. (d) Rate performance. (e) The Charge curves of each sample at 4 C (1 C=300 mA g⁻¹). (f) Long-term cycling stability at 600 mA g⁻¹. (g) Radar plot evaluating the electrochemical properties of the Pristine HC and 3wt%P HC electrodes.

pristine-HC during rate cycling tests may be attributed to continuous electrolyte decomposition caused by an unstable SEI. The galvanostatic charge-discharge (GCD) curves at a high rate (4 C) further indicate that the phosphorized anode delivers a higher reversible capacity (Figure 3e), particularly in the high-voltage region (relative to Na⁺/Na > 0.1 V), where the capacity increases from 105 mAh g⁻¹ (pristine-HC) to 121 mAh g⁻¹ (HC-3wt%P). This suggests that phosphorization enhances the high-voltage reversible adsorption of bamboo powder-derived hard carbon, thereby facilitating rapid Na⁺ transport kinetics.

As for the cyclability shown in Figure S12b (Supporting Information), the HC-3wt%P anode maintains the highest charge-specific capacity of 223 mAh g⁻¹ and the high capacity retention of 87.9% after 450 cycles at a current density of 300 mA g⁻¹. At an elevated current density of 600 mA g⁻¹, the charge-discharge cycling stability exhibits a progressive enhancement with an increase in red phosphorus content, as illustrated in Figure 3f. After undergoing 1000 cycles, the HC-3wt%P anode demonstrates the highest specific capacity of 178 mAh g⁻¹, accompanied by a retention rate of 73.3%. This represents a notable improvement when compared to the

pristine-HC anode, which exhibits a specific capacity of 100 mAh g⁻¹ and a retention rate of 58.9%. Even when subjected to an ultra-high current density of 3 A g⁻¹, the HC-3wt%P anode displays superior stability and specific capacity over the course of 450 cycles, significantly surpassing the performance of the pristine-HC anode (refer to Figure S12c in the Supporting Information). Furthermore, when evaluated at high current rates, the charge-discharge performance of the HC-3wt%P anode displays exceptional cycling stability in comparison to recently reported hard-carbon (HC) anodes (refer to Figure S13 and Table S3 in the Supporting Information). The notable enhancement in cycling stability at high current rates is likely attributable to the initial formation of a more stable interface within the phosphorized hard-carbon anode (a detailed exploration of this phenomenon is provided in the subsequent sections), which is further coupled with a decrease in irreversible side reactions with the electrolyte.

The surface morphology of the hard carbon anode after 10 cycles was scrutinized using SEM and atomic force microscopy (AFM). Figures 4a and 4c present that the Pristine HC anode exhibits significant agglomeration and pronounced surface roughness before
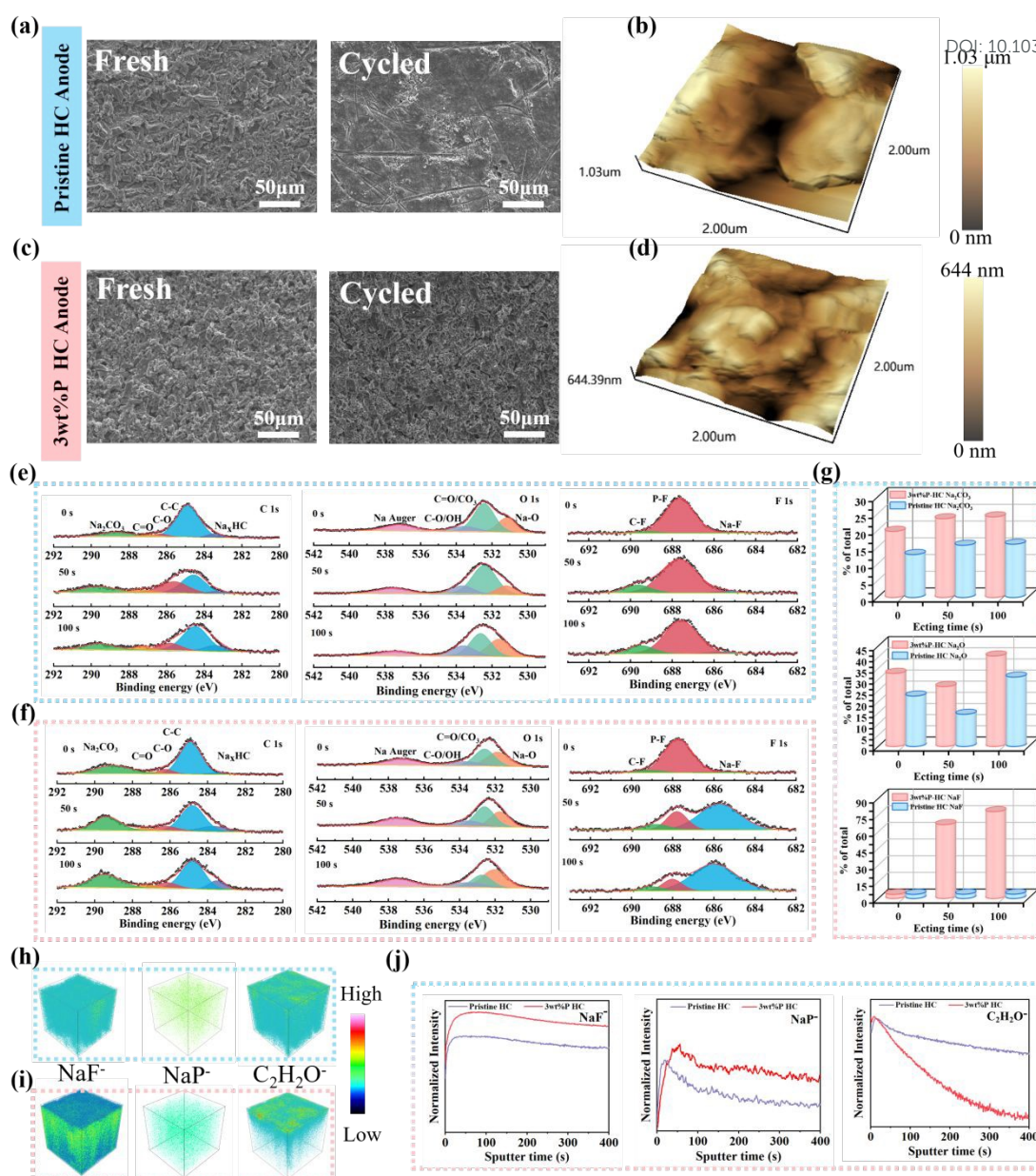
Fig. 4 Characterization of SEI properties from the phosphatized HC and pristine HC anodes. (a, b) SEM and 3D topographical AFM images of fresh and cycled pristine HC anodes. (c, d) SEM and 3D topographical AFM images of fresh and cycled 3wt%P HC anodes. (e, f) Depth-profiling XPS spectra of C 1s, O 1s, and F 1s from the pristine HC and phosphatized HC anodes, respectively. (g) The proportion of SEI components calculated from the C 1s, O 1s, and F 1s spectra. (h, i) 3D distributions of various species secondary ion fragments obtained by sputtering and TOF-SIMS analysis of the pristine HC and phosphatized HC anodes, respectively. (j) The corresponding ionic distributions along the depth profiles.

and after cycling, whereas the HC-3wt%P anode largely retains its original morphology after cycling. The magnified SEM images (Figure S14, Supporting Information) further reveal that the HC-3wt%P anode has fewer surface deposits and a smoother surface. More localized and precise AFM images, as depicted in Figures 4b, 4d reveal that, in contrast to the rough and uneven surface of the Pristine HC anode, the HC-3wt%P anode develops a much smoother surface after cycling, which is in consistent with the aforementioned observations. Based on the observed differences in surface morphology, it can be speculated that compared to pristine hard carbon, the phosphorized hard carbon anode can mitigate side reactions of the electrolyte and suppress its continuous degradation, thereby forming a thinner SEI. The microstructure of the SEI is further

observed through TEM. As shown in Figure 5a, compared to the SEI on the Pristine-HC electrode, which exhibits an uneven thickness (28-50 nm), the SEI observed on the HC-3wt%P electrode is thinner and more uniform (15-22 nm).

Further XPS with varying etching depths was conducted to investigate the structure and composition of the SEI on the HC anode after 10 cycles. By fitting detailed XPS peaks and binding energies, it is determined that while the SEI composition is similar across the samples. the content of its various components varies (Table S4, Supporting Information). Figures 4e and 4f (Figure S16, Supporting Information) present the high-resolution spectra of C 1s, O 1s, F 1s, P 2p, and Na 1s for the Pristine-HC and HC-3wt%P anodes after cycling. In the C 1s spectrum, peaks appear at 284.7 eV (C-C), 286.1
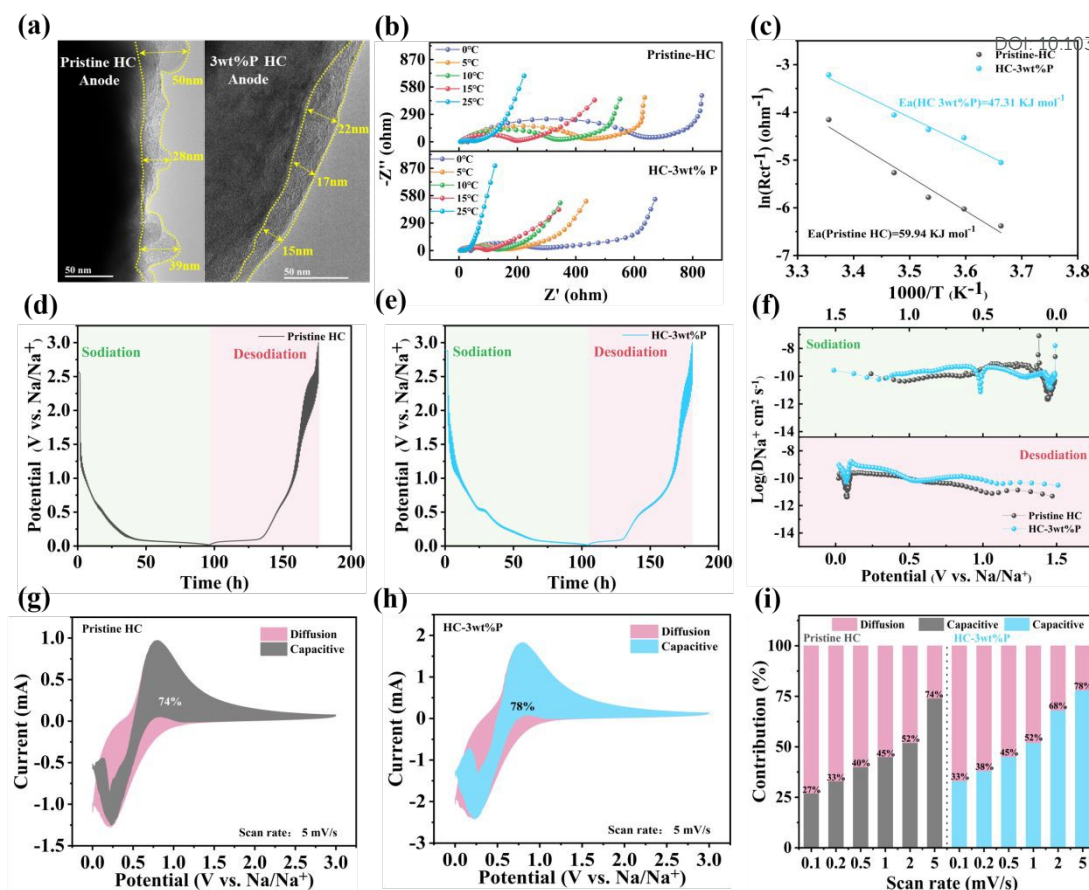
Fig. 5 Electrode kinetic analysis of the phosphatized HC and pristine HC anodes. (a) HRTEM images of cycled anodes. (b) Temperature dependent Nyquist plots of pristine HC and 3wt%P HC electrodes from 273K to 298K. (c) The activation energies for the charge-transfer process. (d, e) GITT curves of pristine HC and phosphatized HC anodes, respectively. (f) The diffusion coefficients of Na$^+$ calculated from the GITT curves. (g, h) Capacitive and diffusion contribution at 5 mV s^{-1} of pristine HC and phosphatized HC anodes. (i) Capacitive contributions at various scanning rates.

eV (C-O), and 286.7 eV (COO), while the O 1s peak at 533.8 eV (C-O/O-H) corresponds to organic components such as ROCO$_2$Na and (CH$_2$OCO$_2$Na)$_2$, which are generated from solvent decomposition. The C 1s peak at 289.7 eV (CO$_3$), the O 1s peak at 531.5 eV (Na-O), and the F 1s peak at 685.5 eV (Na-F) are attributed to the inorganic components Na$_2$CO$_3$, Na$_2$O and NaF, respectively.[42, 45] As the sputtering depth increases, the proportion of inorganic components in the SEI on the HC-3wt%P anode is generally higher than that in the SEI on the Pristine-HC anode (Figure 4g), indicating that the presence of the phosphorization layer facilitates the formation of an SEI rich in inorganic components on the anode surface. Such a structure not only exhibits greater stability but also helps to reduce the continuous consumption of the electrolyte.[18, 19] Furthermore, a higher proportion of inorganic components in the SEI can enhance the conductivity of Na$^+$, which is a crucial for the significantly enhanced rate performance of the HC-3wt%P anode.

Time-of-flight secondary ion mass spectrometry (TOF-SIMS) was utilized to more qualitatively analyze the compositional distribution within the SEI. As shown in Figures 4h, 4i, S17 and S18 (Supporting Information), ion fragments corresponding to relevant inorganic components, including NaF$^-$, NaP$^-$, NaCO$_3^-$ and NaO$^-$ were detected. Meanwhile, the C$_2$H$_2$O$^-$ fragment was attributed to organic compounds.[46] The NaP$^-$ fragment content is consistently higher across the surface of the HC-3wt%P anode compared to the Pristine-

HC anode (Figure 4j). This is associated with the preferential formation of Na$_3$P during the initial discharge stage due to the interaction between the phosphorization layer and sodium metal. Additionally, the NaF$^-$ fragment also exhibits a higher concentration on the surface of the HC-3wt%P anode. In contrast, the C$_2$H$_2$O$^-$ fragment is primarily concentrated on the surface of the HC-3wt%P anode, with a significantly reduced presence at greater depths. The quantitative statistical results from the 3D visual maps indicate that for the cycled phosphorized anode, inorganic components are abundant and dominate the entire SEI, while organic components are present in lower amounts and are mainly distributed on the outer surface of the SEI. The combination of a thinner, inorganic-rich, and chemically uniform SEI facilitates the formation of a homogeneous Na$^+$ diffusion channel on the HC anode surface.[35, 40] EDS mapping further confirms that the distribution of Na in the cycled phosphorized anode is more uniform (Figure S19, Supporting Information).

The inorganic-rich and thinner SEI structure has an impact on the kinetics of sodium ion transport and storage. Based on electrochemical impedance spectroscopy (EIS) measurements (Figure 5b and Figure S20, Supporting Information), the HC-3wt%P anode exhibits the smallest charge transfer resistance (Rct). The as-calculated Warburg factor (σ) value for HC-3wt%P (32.9) is significantly lower than that for Pristine-HC (69.3), indicating
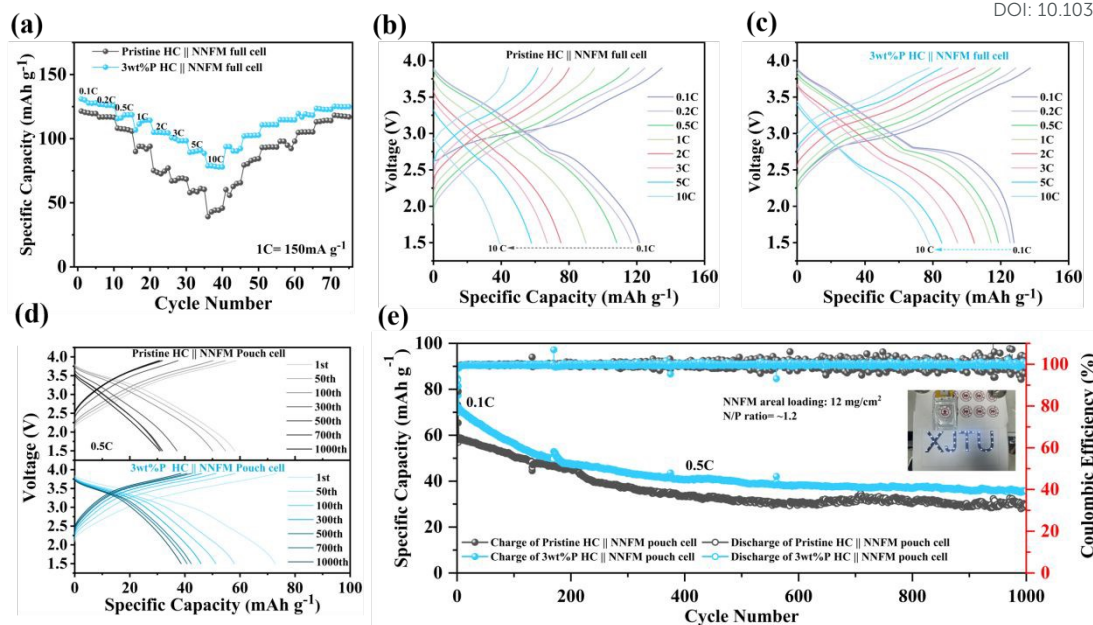
Fig. 6 Electrochemical performances of 3wt%P HC and Pristine HC//NNFM full cell. (a) Rate capability. (b, c) At different current densities, the GCD profiles of Pristine HC and 3wt%P HC/NNFM full cell, respectively. (d) GCD curves of Pristine HC and 3wt%P HC/NNFM pouch cell during the different cycles at 0.5 C. (e) Long term cycling stability of pouch cells at 0.5 C for 1000 cycles (The illustration shows the practical scene of lighting LED lamps with pouch cell).

superior electrochemical kinetics. [47]

Temperature-dependent EIS measurements were conducted to obtain the Na$^+$ transport and charge transfer resistances across the SEI, and the apparent activation energy for Na$^+$ transport was calculated using the Arrhenius law (Equation 1).[48] The activation energy for Na$^+$ transport across the SEI and charge transfer at the HC-3wt%P anode (Figure 5c) is 47.31 kJ mol^{-1}, lower than that for the Pristine-HC anode (59.94 kJ mol^{-1}), indicating that the Na$^+$ diffusion kinetics at the interface and within the SEI are improved on the phosphated anode surface.

$$\sigma T = A exp(- E_a / k_B T) \qquad (1)$$

Where k is the reaction rate constant, A is the pre-exponential factor, R represents the molar gas constant and T is the absolute temperature.

Furthermore, according to the galvanostatic intermittent titration technique (GITT) tests (Figures 5d, 5e and S21, Supporting Information) the Na$^+$ diffusion coefficient for the HC-3wt%P anode is higher compared to the Pristine-HC anode (Figure 5f) attributing to the enhance electrode-electrolyte affinity as well as the as-formed inorganic-rich SEI originated from the well-designed the phosphating layer.

A kinetic analysis of the fast-charging performance improvement in the half-cell was conducted through varying scan rate cyclic voltammetry (CV) tests. Analysis of the CV curves for the first three cycles at a scan rate of 0.1 mV s^{-1} (Figure S22, Supporting Information) reveals that the area enclosed by the phosphated anode's curves is generally larger, indicating more Na$^+$ undergo reversible migration during the charge-discharge process. This further supports the higher reversible capacity observed in the previous GCD tests. Pseudocapacitive current contributions were fitted using the surface-controlled and diffusion-controlled formulas (Figure S23, Supporting Information) based on CV curves obtained at

scan rates of 0.1, 0.2, 0.5, 1, 2, and 5 mV s^{-1}.[49] As shown in Figures 5g and 5h, the capacitive contribution increases significantly with the scan rate. At a scan rate of 5 mV s^{-1}, the capacitive current contribution of the HC-3wt%P anode is 78%, which is higher than that of the Pristine-HC anode at 74% (Figure 5i). These results confirm that, during high-rate charge/discharge processes, the HC-3wt%P anode exhibits superior fast sodium storage kinetics.

Last but not the least, to assess the commercialization prospects of the phosphated bamboo powder-based hard carbon anode, sodium-ion full cells were assembled with Pristine-HC and HC-3wt%P as anodes and O3-NaNi$_{1/3}$Fe$_{1/3}$Mn$_{1/3}$O$_2$ (NNFM) as the cathode for electrochemical testing. As shown in Figure S24 (Supporting Information), the full cell provides a high reversible capacity of 125 mAh g^{-1} within a current rate of 0.1C and a voltage window of 1.5-3.9 V (1 C = 150 mA g^{-1}).[50] Figure 6a shows that the assembled full cell achieves highly reversible rate performance (0.1 C-10 C-0.1 C). The HC-3wt%P//NNFM full cell provides a reversible capacity of 78 mAh g^{-1} at a high rate of 10C, which is significantly better than the 10C performance (45 mAh g^{-1}) of the Pristine-HC//NNFM full cell. Figures 6b and 6c reveal that, during high current charge/discharge, the Pristine-HC//NNFM full cell experiences significant electrochemical polarization, leading to a substantial capacity decay. After 100 cycles at 2 C, the HC-3wt%P-assembled full cell maintains more stable charge/discharge behavior, with a capacity retention rate of 81.8% (Figures S25a-c, Supporting Information).

Furthermore, pouch cells featuring a high-loading cathode (~12 mg cm^{-2}). Rate tests at 0.1 C-2 C also confirm that the phosphated anode indeed improves the fast-charging performance of the pouch cell (Figures S25d-f, Supporting Information). Long-cycle testing performed at a 0.5 C rate verified that the full cell incorporating the phosphated anode demonstrates more stable cycling behavior and delivers a higher discharge capacity. The inset in the figure illustrates

the pouch cell illuminating the XJTU logo (as shown in Figures 6d and 6e). This demonstrates its potential for practical applications.

Conclusions

In summary, a strategy is proposed to enhance the fast-charging performance of bamboo-derived hard carbon by constructing a phosphating layer. The phosphating layer on the surface of bamboo-derived hard carbon can induce the formation of a SEI-riched in inorganic components such as Na_3P and NaF, which can effectively suppress continuous side reactions between the electrode and the electrolyte and reduce the impedance during charging and discharging to improve the efficiency of the battery. Moreover, as Na_3P near the inner Helmholtz plane (IHP) can promote the formation of a solvation shell with a low solvent coordination number can form, the Na^+ desolvation capability as well as the conductivity can be strengthened accordingly. Which facilitates the rapid storage capacity of sodium ions in high voltage region (> 0.1 V) to improve the rate performance. Among the designed gradient-phosphated hard carbon anodes, the HC-3wt%P anode exhibits the best Na^+ storage performance and excellent rate capability in half-cell performance tests. Furthermore, a pouch cell assembled with the corresponding cathode demonstrates stable cycling for 1000 cycles at 0.5 C. The phosphating layer construction on bamboo powder-based hard carbon proposed in this study provides meaningful guidance for rationally improving the SEI on the anode side to bridge the gap between interfacial chemistry and fast-charging performance.

Data availability

The data supporting this article have been included as part of the ESI.†

Author contributions

Haihan Zhang: writing-original draft, methodology, investigation, data curation. Zhenxin Huang: software, investigation. Siyuan Lin: data curation, manuscript revision. Jiawu Cui: data curation, investigation. Qianyu Zhang: supervision. Xiansheng Luo: data curation. Rui Wang: data curation. Chaofeng Zhang: formal analysis. Chengyong Shu: supervision, project administration. Wei Tang: writing-review & editing, supervision, project administration, funding acquisition.

Conflicts of interest

There are no conflicts to declare.

Acknowledgements

References

1   R. Usiskin, Y. Lu, J. Popovic, M. Law, P. Balaya, Y.-S. Hu and J. Maier, Fundamentals, status and promise of sodium-based batteries, *Nat. Rev. Mater.*, 2021, **6**, 1020-1035.

2   F. Wang, Z. Jiang, Y. Zhang, Y. Zhang, J. Li, H. Wang, Y. Jiang, G. Xing, H. Liu and Y. Tang, Revitalizing sodium-ion batteries via controllable microstructures and advanced electrolytes for hard carbon, *eScience*, 2024, **4**, 100181.

3   Y.-F. Sun, Y. Li, Y.-T. Gong, Z.-X. Qiu, J. Qian, Y. Bai, Z.-L. Wang, R.-P. Zhang and C. Wu, Constructing three-dimensional architectures to design advanced anodes materials for sodium-ion batteries: from nanoscale to microscale, *Energy Mater.*, 2024, **4**, 400002.

4   L. Liu, L. Xiao, Z. Sun, S. Bashir, R. Kasi, Y. Gu and R. Subramaniam, Rational manipulation of electrolyte to induce homogeneous SEI on hard carbon anode for sodium-ion battery, *J. Energy Chem.*, 2024, **94**, 414-429.

5   Y. Guo, S. Ji, F. Liu, Z. Zhu, J. Xiao, K. Liu, Y. Zhang, S. Liao and X. Zeng, A review of the preparation and characterization techniques for closed pores in hard carbon and their functions in sodium-ion batteries, *Energy Mater.*, 2025, **5**, 500030.

6   Y. Wan, B. Huang, W. Liu, D. Chao, Y. Wang and W. Li, Fast-Charging Anode Materials for Sodium-Ion Batteries, *Adv. Mater.*, 2024, **36**, 2404574.

7   B. Zhong, C. Liu, D. Xiong, J. Cai, J. Li, D. Li, Z. Cao, B. Song, W. Deng, H. Peng, H. Hou, G. Zou and X. Ji, Biomass-Derived Hard Carbon for Sodium-Ion Batteries: Basic Research and Industrial Application, *ACS Nano*, 2024, **18**, 16468-16488.

8   S. Zhou, Z. Tang, Z. Pan, Y. Huang, L. Zhao, X. Zhang, D. Sun, Y. Tang, A. S. Dhmees and H. Wang, Regulating closed pore structure enables significantly improved sodium storage for hard carbon pyrolyzing at relatively low temperature, *SusMat*, 2022, **2**, 357-367.

9   C. Wu, Y. Yang, Y. Zhang, H. Xu, W. Huang, X. He, Q. Chen, H. Dong, L. Li, X. Wu and S. Chou, Industrial-Scale Hard Carbon Designed to Regulate Electrochemical Polarization for Fast Sodium Storage, *Angew. Chem. Int. Ed.*, 2024, **63**, e202406889.

10   H. Zhang, M. Yang, Z. Xiao, K. Xie, L. Shao, C. Huang, C. Shu, C. Peng, Y. Wu and W. Tang, Flexible Precursor Modulation toward Selective Heteroatom Doping in a Hard-Carbon Anode for Sodium-Ion Batteries, *Energy Fuels*, 2023, **37**, 15127-15137.

11   J. Cui, P. Su, W. Li, X. Wang, Y. Zhang, Z. Xiao, Q. An and Z. Chen, Advanced Cellulose-Derived Hard Carbon as Anode for Sodium-Ion Batteries: Mechanisms, Optimization, and Challenges, *Adv. Energy Mater.*, 2025, **15**, 2404604.

12   T. Zhang, T. Zhang, C. Zhao, F. Wang, L. Zhang, Y. Li, L. Zhang and F. Ran, Revealing Effect of Aggregation Structure of Plant Precursors on Rate Performance of Carbon Anode for Sodium-

Ion Batteries, *Adv. Funct. Mater.*, 2025, DOI: 10.1002/adfm.202425234, 2425234.

13   H. Zhang, S. Lin, C. Shu, Z. Tang, X. Wang, Y. Wu and W. Tang, Advances and perspectives of hard carbon anode modulated by defect/hetero elemental engineering for sodium ion batteries, *Mater. Today*, 2025, **85**, 231-252.

14   M. H. Song, Q. Song, T. Zhang, X. M. Huo, Z. Z. Lin, Z. W. Hu, L. Dong, T. Jin, C. Shen and K. Y. Xie, Growing curly graphene layer boosts hard carbon with superior sodium-ion storage, *Nano Research*, 2023, **16**, 9299-9309.

15   Y. Li, Q. Zhou, S. Weng, F. Ding, X. Qi, J. Lu, Y. Li, X. Zhang, X. Rong, Y. Lu, X. Wang, R. Xiao, H. Li, X. Huang, L. Chen and Y.-S. Hu, Interfacial engineering to achieve an energy density of over 200 Wh kg−1 in sodium batteries, *Nature Energy*, 2022, **7**, 511-519.

16   W. Kuang, X. Zhou, Z. Fan, X. Chen, Z. Yang, J. Chen, X. Shi, L. Li, R. Zeng, J.-Z. Wang and S. Chou, Sulfur-Containing Inorganic-Rich Interfacial Chemistry Empowers Advanced Sodium-Ion Full Batteries, *ACS Energy Lett.*, 2024, **9**, 4111-4118.

17   Y. Wang, Z. Yi, L. Xie, Y. Mao, W. Ji, Z. Liu, X. Wei, F. Su and C. M. Chen, Releasing Free Radicals in Precursor Triggers the Formation of Closed Pores in Hard Carbon for Sodium‐Ion Batteries, *Adv. Mater.*, 2024, **36**, 2401249.

18   S. Tu, B. Zhang, Y. Zhang, Z. Chen, X. Wang, R. Zhan, Y. Ou, W. Wang, X. Liu, X. Duan, L. Wang and Y. Sun, Fast-charging capability of graphite-based lithium-ion batteries enabled by Li3P-based crystalline solid–electrolyte interphase, *Nature Energy*, 2023, **8**, 1365-1374.

19   Y. Liao, L. Yuan, Y. Han, C. Liang, Z. Li, Z. Li, W. Luo, D. Wang and Y. Huang, Pentafluoro(phenoxy)cyclotriphosphazene Stabilizes Electrode/Electrolyte Interfaces for Sodium-Ion Pouch Cells of 145 Wh Kg(-1), *Adv Mater*, 2024, **36**, e2312287.

20   S. You, Q. Zhang, J. Liu, Q. Deng, Z. Sun, D. Cao, T. Liu, K. Amine and C. Yang, Hard carbon with an opened pore structure for enhanced sodium storage performance, *Energy Environ. Sci.*, 2024, **17**, 8189-8197.

21   Y.-C. Tan, W.-W. Liu, W.-Y. Wang, X.-X. Liu, J.-M. Du and Y.-M. Sun, Embedment of red phosphorus in anthracite matrix for stable battery anode, *Rare Met.*, 2022, **41**, 2819-2825.

22   Y. Zeng, F. Wang, Y. Cheng, M. Chen, J. Hou, D. Yang, Y. Zhang, W. Yang, G. Liu, Y. Zhang, Z. Zhu, X. Li, Y. Yang and J. Zhao, Identifying the importance of functionalization evolution during pre-oxidation treatment in producing economical asphalt-derived hard carbon for Na-ion batteries, *Energy Storage Mater.*, 2024, **73**, 103808.

23   Z. G. Liu, J. Zhao, H. Yao, X. X. He, H. Zhang, Y. Qiao, X. Q. Wu, L. Li and S. L. Chou, P-doped spherical hard carbon with high initial coulombic efficiency and enhanced capacity for sodium ion batteries, *Chem Sci*, 2024, **15**, 8478-8487.

24   K.-Y. Zhang, H.-H. Liu, J.-M. Cao, J.-L. Yang, M.-Y. Su, X.-Y. Wang, Z.-Y. Gu, J. Wang, B. Li, Y. Wang and X.-L. Wu, Microstructure reconstruction via confined carbonization achieves highly available sodium ion diffusion channels in hard carbon, *Energy Storage Mater.*, 2024, **73**, 103839.

25   Q. Hu, L. Xu, G. Liu, J. Hu, X. Ji and Y. Wu, Understanding the Sodium Storage Behavior of Closed Pores/Carbonyl Groups in Hard Carbon, *ACS Nano*, 2024, **18**, 21491-21503.

26   Y. Fang, L. Li, J. Li, Y. Gan, J. Du, J. Li, X. Chen, H. Pan, W. Zhang, J. Gu, D. Zhang and Q. Liu, Ultrafast High‐Volumetric Sodium‐Ion Capacitors Based on Compact Nanoarchitectured Carbon Electrodes, *Adv. Funct. Mater.*, 2024, **34**, 2408568

27   J. Peng, H. Wang, X. Shi and H. J. Fan, Ultrahigh Plateau‐Capacity Sodium Storage by Plugging Open Pores, *Adv. Mater.*, 2024, DOI: 10.1002/adma.202410326, 2410326

28   Z. Huang, J. Huang, L. Zhong, W. Zhang and X. Qiu, Deconstruction Engineering of Lignocellulose Toward High‐Plateau‐Capacity Hard Carbon Anodes for Sodium‐Ion Batteries, *Small*, 2024, **20**, 2405632

29   Z. Zheng, S. Hu, W. Yin, J. Peng, R. Wang, J. Jin, B. He, Y. Gong, H. Wang and H. J. Fan, CO2‐Etching Creates Abundant Closed Pores in Hard Carbon for High‐Plateau‐Capacity Sodium Storage, *Adv. Energy Mater.*, 2023, **14**, 2303064.

30   J. Yan, H. Li, K. Wang, Q. Jin, C. Lai, R. Wang, S. Cao, J. Han, Z. Zhang, J. Su and K. Jiang, Ultrahigh Phosphorus Doping of Carbon for High‐Rate Sodium Ion Batteries Anode, *Adv. Energy Mater.*, 2021, **11**, 2003911.

31   L. Wang, A. Menakath, F. Han, Y. Wang, P. Y. Zavalij, K. J. Gaskell, O. Borodin, D. Iuga, S. P. Brown, C. Wang, K. Xu and B. W. Eichhorn, Identifying the components of the solid–electrolyte interphase in Li-ion batteries, *Nat. Chem.*, 2019, **11**, 789-796.

32   C. Yang, W. Zhong, Y. Liu, Q. Deng, Q. Cheng, X. Liu and C. Yang, Regulating solid electrolyte interphase film on fluorine‐doped hard carbon anode for sodium‐ion battery, *Carbon Energy*, 2024, **6**, 503.

33   P. Liu, L. Miao, Z. Sun, X. Chen and L. Jiao, Sodiophilic Substrate Induces NaF‐Rich Solid Electrolyte Interface for Dendrite‐Free Sodium Metal Anode, *Adv. Mater.*, 2024, DOI: 10.1002/adma.202406058, 2406058

34   L. Chen, M. Chen, Q. Meng, J. Zhang, G. Feng, X. Ai, Y. Cao and Z. Chen, Reconstructing Helmholtz Plane Enables Robust F‐Rich Interface for Long‐Life and High‐Safe Sodium‐Ion Batteries, *Angew. Chem. Int. Ed.*, 2024, **63**, e202407717

35   Y. H. Feng, M. Liu, W. Qi, H. Liu, Q. Liu, C. Yang, Y. Tang, X. Zhu, S. Sun, Y. M. Li, T. L. Chen, B. Xiao, X. Ji, Y. You and P. F. Wang, Dual‐Anionic Coordination Manipulation Induces Phosphorus and Boron‐Rich Gradient Interphase Towards Stable and Safe Sodium Metal Batteries, *Angew. Chem. Int. Ed.*, 2024, **64**, e202415644.

36   Z. Huang, Z. Xiao, H. Zhang, Q. Zhang, J. Cui, J. Luo, W. Tang and Y. Wu, Temperature-Robust Solvation Enabled by Solvent Interactions for Low-Temperature Sodium Metal Batteries, *J. Am. Chem. Soc.*, 2025, **147**, 5162-5171.

37   X. Hou, S. Wang, B. Wang, Y. Qiu, M. Jiang, Y. Tang, Q. Zheng and X. Li, Electrolyte Reconfiguration by Cation/Anion Cross‐coordination for Highly Reversible and Facile Sodium Storage, *Angew. Chem. Int. Ed.*, 2024, **64**, e202416939.

38   Y. Liu, S. Yang, H. Guo, Z. Wang, J. Liu, N. Chen and X. Gong, Low LUMO energy carbon molecular interface to suppress electrolyte decomposition for fast charging natural graphite anode, *Energy Storage Mater.*, 2024, **73**, 103806.

39   S. Zhao and F. Huang, Weakly Solvating Few-Layer-Carbon Interface toward High Initial Coulombic Efficiency and Cyclability Hard Carbon Anodes, *ACS Nano*, 2024, **18**, 1733-1743.

40   S. Ma, J. Zhao, H. Xiao, Q. Gao, F. Li, C. Song and G. Li, Modulating the Inner Helmholtz Plane towards Stable Solid Electrolyte Interphase by Anion‐π Interactions for High‐Performance Anode‐Free Lithium Metal Batteries, *Angew. Chem. Int. Ed.*, 2024, **64**, e202412955.

41   X. Liu, M. Zhang, X. Wang, Y. Peng, Y. Liu, S. Ullah, Z. Duan, W. Gao, B. Song, M. Wei, J. He, Z. Li and Y. Wu, Evidence of Quasi‐Na Metallic Clusters in Sodium Ion Batteries through In Situ X‐Ray Diffraction, *Adv. Mater.*, 2024, **37**, 2410673

42   M. Liu, F. Wu, Y. Gong, Y. Li, Y. Li, X. Feng, Q. Li, C. Wu and Y. Bai, Interfacial Catalysis Enabled Layered and Inorganic-Rich SEI on Hard Carbon Anodes in Ester Electrolytes for Sodium-Ion Batteries, *Adv. Mater.*, 2023, **35**, e2300002.

43   Y. Aniskevich, J. H. Yu, J. Y. Kim, S. Komaba and S. T. Myung, Tracking Sodium Cluster Dynamics in Hard Carbon with a Low Specific Surface Area for Sodium‑Ion Batteries, *Adv. Energy Mater.*, 2024, **14**, 2304300.

44   J. C. Hyun, H. M. Jin, J. H. Kwak, S. Ha, D. H. Kang, H. S. Kim, S. Kim, M. Park, C. Y. Kim, J. Yoon, J. S. Park, J.-Y. Kim, H.-D. Lim, S. Y. Cho, H.-J. Jin and Y. S. Yun, Design guidelines for a high-performance hard carbon anode in sodium ion batteries, *Energy Environ. Sci.*, 2024, **17**, 2856-2863.

45   H. Zhang, L. Song, S. Lin, Z. Huang, C. Shu, Y. Ma, Z. Tang, X. Wang, W. Tang and Y. Wu, Ameliorating the sodium storage performance of hard carbon anode through rational modulation of binder, *Energy Storage Mater.*, 2024, **73**, 103796.

46   Y. Dong, Y. Chen, X. Yue and Z. Liang, Unveiling the adsorption tendency of film-forming additives to enable fast-charging hard carbon anodes with regulated Li plating, *Energy Environ. Sci.*, 2024, **17**, 2500-2511.

47   Y. Zhao, Z. Hu, W. Zhou, P. Gao, Z. Liu, J. Liu, C. Fan and J. Liu, Advanced Structural Engineering Design for Tailored Microporous Structure via Adjustable Graphite Sheet Angle to Enhance Sodium‑Ion Storage in Anthracite‑Based Carbon Anode, *Adv. Funct. Mater.*, 2024, DOI: 10.1002/adfm.202405174, 2405174.

48   Z. Y. Lu, H. J. Yang, Y. Guo, H. X. Lin, P. Z. Shan, S. C. Wu, P. He, Y. Yang, Q. H. Yang and H. S. Zhou, Consummating ion desolvation in hard carbon anodes for reversible sodium storage, *Nat. Commun.*, 2024, **15**, 3497.

49   Y. Zhou, Y. Wang, C. Fu, J. Zhou, Y. Song, S. Lin, S. Liang, S. Zhou and A. Pan, Tailoring Pseudo‑Graphitic Domain by Molybdenum Modification to Boost Sodium Storage Capacity and Durability for Hard Carbon, *Small*, 2024, **20**, 2405921.

50   M. Fei, L. Qi, S. Han, Y. Li, H. Xi, Z. Lin, J. Wang, C. Ducati, M. Chhowalla, R. V. Kumar, Y. Jin and J. Zhu, Preformation of Insoluble Solid‑Electrolyte Interphase for Highly Reversible Na‑Ion Batteries, *Angew. Chem. Int. Ed.*, 2024, **63**, e202409719

Chemical Science Accepted Manuscript

Rational phosphating layer design in biomass-derived hard carbons toward fast charging capability of sodium ion battery anodes

The data underlying this study are available in the published article and its ESI,† or available from the authors on request.